

# UC Berkeley

## UC Berkeley Previously Published Works

### Title

Electrode roughness dependent electrodeposition of sodium at the nanoscale

### Permalink

<https://escholarship.org/uc/item/9c96v8xd>

### Authors

Zeng, Z  
Barai, P  
Lee, SY  
[et al.](#)

### Publication Date

2020-06-01

### DOI

10.1016/j.nanoen.2020.104721

### Copyright Information

This work is made available under the terms of a Creative Commons Attribution-NonCommercial-NoDerivatives License, available at <https://creativecommons.org/licenses/by-nc-nd/4.0/>

Peer reviewed

## Electrode Roughness Dependent Electrodeposition of Sodium at the Nanoscale

Zhiyuan Zeng,<sup>1,2</sup> Pallab Barai,<sup>3</sup> Seung-Yong Lee,<sup>1</sup> Juan Yang,<sup>1</sup> Xiaowei Zhang,<sup>1</sup> Wenjing Zheng,<sup>1</sup>  
Yi-Sheng Liu,<sup>4</sup> Karen C. Bustillo,<sup>5</sup> Peter Ercius,<sup>5</sup> Jinghua Guo,<sup>4,6</sup> Yi Cui,<sup>7,8\*</sup> Venkat Srinivasan,<sup>3</sup>  
Haimei Zheng<sup>1,9\*</sup>

<sup>1</sup>*Materials Sciences Division, Lawrence Berkeley National Laboratory, Berkeley, CA 94720, USA*

<sup>2</sup>*Department of Materials Science and Engineering, City University of Hong Kong, Kowloon, Hong Kong, China*

<sup>3</sup>*Energy Systems Division, Argonne National Laboratory, Lemont, IL USA*

<sup>4</sup>*Advanced Light Source, Lawrence Berkeley National Laboratory, Berkeley, CA 94720, USA;*

<sup>5</sup>*National Center for Electron Microscopy, Molecular Foundry, Lawrence Berkeley National Laboratory, Berkeley, California 94720, United States*

<sup>6</sup>*Department of Chemistry and Biochemistry, University of California, Santa Cruz, California 95064, USA*

<sup>7</sup>*Department of Materials Science and Engineering, Stanford University, Stanford, California 94305, United States*

<sup>8</sup>*Stanford Institute for Materials and Energy Sciences, SLAC National Accelerator Laboratory, Menlo Park, California 94025, United States*

<sup>9</sup>*Department of Materials Science and Engineering, University of California, Berkeley, CA 94720, USA*

**\*Correspondence to:** *hmzheng@lbl.gov (HZ) and yicui@stanford.edu (YC)*

**Keywords:** liquid cell TEM, electrochemical liquid cell, Na deposition, solid electrolyte interface, sodium ion batteries.

**Abstract:**

Na metal is an attractive anode material for rechargeable Na ion batteries, however, the dendritic growth of Na can cause serious safety issues. Along with modifications of solid-electrolyte interphase (SEI), engineering the electrode has been reported to be effective in suppressing Na dendritic growth, likely by reducing localized current density accumulation. However, fundamental understanding of Na growth at the nanoscale is still limited. Here, we report an *in-situ* study of Na electrodeposition in electrochemical liquid cells with the electrodes in different surface roughness, e.g., flat or sharp curvature. Real time observation using transmission electron microscopy (TEM) reveals the Na electrodeposition with remarkable details. Relatively large Na grains (in the micrometer scale) are achieved on the flat electrode surface. The local SEI thickness variations impact the growth rate, thus the morphology of individual grains. In contrast, small Na grains (in tens of nanometers) grow explosively on the electrode at the point with sharp curvature. The newly formed Na grains preferentially deposit at the base of existing grains close to the electrode. Further studies using continuum-based computational modeling suggest that the growth mode of an alkali metal (e.g. Na) is strongly influenced by the transport properties of SEI. Our direct observation of Na deposition in combination with the theoretical modeling provides insights for comprehensive understanding of electrode roughness and SEI effects on Na electrochemical deposition.

## 1. Introduction

The ever-increasing demand for batteries and capacitors with better performance and low cost has spurred intense interests on various research themes, such as, the exploration of alternative chemistry beyond lithium, effective electrode materials, and *in-situ* diagnostic methods to analyze the performance of electrochemical devices [1-5]. Na-ion batteries with the earth abundant element have attracted wide attention for large-scale energy storage applications [6-10]. Na metal is an attractive anode material for rechargeable Na-based batteries due to its high specific capacity ( $1165 \text{ mAhg}^{-1}$ ) and low working potential compared to other anode materials. Nevertheless, the dendritic growth of Na metal can result in premature cell failure [11].

The dendritic growth of Na is often considered as an issue analogous to that of Li. However, recent reports have acknowledged the fundamental differences. For example, Na has a much larger radius (by more than 30%), a greater mass (by more than 3 times), a different reduction potential ( $\sim 0.33 \text{ V vs Li/Li}^+$ ), different mechanical properties, etc. [6, 12, 13]. In addition, Na metal is more reactive than Li and it reacts with carbonate electrolytes in different ways from how Li metal does [14, 15]. Therefore, the study of Na electrodeposition to suppress the dendritic (or mossy) growth arises as a topic with excitement and novelty [12, 16].

Electrode engineering has been explored to suppress Na dendrite formation [12]. For example, it was found that highly porous materials are effective and the suppression of dendritic growth was attributed to the reduced effective current density by their large surface area [17-19]. In addition, the high surface area may also enhance the nucleation of Na and refine the growth front [12, 19, 20]. However, it still lacks fundamental understanding on the impacts of electrode roughness and local current density variations on Na electrodeposition. For example, it was considered that a rough Na metal leads to uneven solid-electrolyte interphase (SEI), thus the ion flux becomes more

concentrated at the protuberance, eventually generating a dendrite [12, 21]. On the contrary, other studies claimed that a geometrically non-uniform metal surface is insignificant to dendrite formation since SEI is intrinsically heterogeneous [12, 22]. There also have been reports that the current collector non-uniformity, which may be introduced by mechanical scratches from processing, dislocation termination on the surfaces, grain boundaries, etc., plays an important role in dendrite formation [12, 21, 23, 24].

Here, we investigate the electrochemical deposition of Na using *in-situ* electrochemical liquid cell transmission electron microscopy (TEM) by simply patterning the electrodes with different curvatures. We compare the electrochemical deposition of Na on the flat and the sharp curved electrodes to explore the impact of electrode surface roughness on the growth dynamics of Na at the nanoscale. The development of electrochemical cells for TEM has enabled the direct observation of many electrochemical processes of Li previously [25-27]. For instance, inhomogeneous nucleation, dynamic growth of Li dendrites, gas bubble generation from electrolyte decomposition, and Li SEI formation in a nano-battery cell have been revealed [27-29]. However, *in-situ* studies of Na electrodeposition using liquid cell TEM have not been achieved so far. Our *in-situ* experiments combined with continuum-based calculations allow for fundamental understanding of Na growth behavior on electrodes with different surface roughness. The finding may assist the future electrode engineering to induce homogeneous Na growth.

## 2. Materials and Methods

### 2.1. Electrochemical liquid TEM cell fabrication

As shown in Fig. 1, we developed electrochemical liquid cells, in which the electrodes were made with different surface roughness. The electrochemical liquid cells were fabricated using Si

wafers with 25 nm thick low stress silicon nitride film as the membrane for imaging. The overall dimensions of a cell are  $\sim 3 \text{ mm} \times 3 \text{ mm} \times 400 \text{ }\mu\text{m}$  (L $\times$  W $\times$  H). Two 90 nm-thick Ti electrodes were deposited on the bottom chip of a liquid cell with a face-to-face distance of 20  $\mu\text{m}$ . Due to the limited space inside the liquid cell, it lacks a reference electrode and thus the counter electrode also worked as the reference electrode. 1M sodium hexafluorophosphate ( $\text{NaPF}_6$ ) dissolved in propylene carbonate (PC) was used as the electrolyte. The liquid electrolyte was loaded into one of the reservoirs using a syringe inside a glovebox. The electrolyte flowed into the viewing window by capillary force. The liquid cell was sealed using Cu foil and epoxy. Such a self-contained nano-battery cell was put into a custom-made TEM holder for *in-situ* TEM experiments. The working and counter electrodes were bonded with aluminum wires connecting with the TEM holder tip/electrochemical workstation for *in-situ* TEM experiments.

## 2.2. *In-situ* TEM measurement

JEOL 2100 TEM microscope operated at 200 kV was used for *in-situ* TEM experiments, which was equipped with a Gatan Orius camera facilitated frame rates of 30 fps and a Direct Electron detector with frame rate up to 400 fps (DE-12, provided by Direct Electron, LP at San Diego, CA). The electrochemical process was controlled by an electrochemical workstation (CH Instruments: Model 660D series). HAADF-STEM images were acquired using an FEI Titan microscope operated at 300 kV with a convergence semi-angle of 10 mrad and an inner half collection angle of 63 mrad. EDS spectra were collected using the FEI Super-X Quad windowless EDS detector with silicon drift technology and a solid angle of 0.7 steradian. A beam current of 600 pA was maintained. Experimental details of *in-situ* x-ray absorption spectroscopy (XAS) and methodology of theoretical continuum analysis are described in Supplementary Materials.

### 3. Results and Discussion

#### 3.1. Na electrodeposition on a flat electrode

We trace the nucleation and growth of Na frame-by-frame from the *in-situ* movies. The size and shape evolution of Na grains during deposition and dissolution on an electrode with flat curvature is shown in Fig. 2A (also see Movie S1). A low electron dose ( $<1\text{e}\cdot\text{\AA}^{-2}\cdot\text{s}^{-1}$ ) was used during imaging to reduce beam-sample interactions. The corresponding applied electrical potential and measured electrical current are plotted in Fig. 2B. Initially, we observe a smooth interface between the Ti electrode and the electrolyte. When a negative potential in cyclic voltammetry is applied on the Ti working electrode, a Na grain (marked as I) nucleates at the edge of the electrode. Concurrently, gas bubbles emerge along the edge of the Ti electrode (at 8.50 s). The bubbles appear to be the gaseous products, such as  $\text{CO}_2$  [30, 31] and  $\text{PF}_5$ , from the electrolyte reduction reactions at the electrode (more discussions are provided in Supplementary Materials). During the gas evolution, we did not encounter any issue of electrolyte leaking into the vacuum, which probably benefits from that the electrochemical cell design has two large reservoirs (see Supplementary Materials). The Na grain grows rapidly and spreads out on the electrode surface. When the applied voltage reaches -1.57 V (at 31.5 s), another Na grain (marked as II) forms while the radius of the first Na grain reaches 800 nm. The electrolyte decomposition at the edge of electrode may lead to SEI formation, as indicated by the white arrows in the frame at 77.5 s. At 78 s, a third Na grain (marked as III) nucleates on the electrode.

During the reverse voltage scan from -4 V to -2.63 V, the three Na grains remain on the electrode. When the voltage changes from negative to positive, the Na grains start to dissolve. At +0.8 V (186 s), vigorous dissolution occurs, and all Na grains and deposits disappear by 224 s.

The size evolution of three Na grains as a function of time is plotted in Fig. 2C. The period for the nucleation and growth of each grain is (I) 8.5-28.5 s, (II) 31.5-59.5 s and (III) 78-102.5 s respectively, indicating the sequential formation behavior. While all three grains are dissolved under positive bias in approximately the same time within 178.5-189.5 s.

We quantify the SEI effects on the kinetics of Na deposition. The SEI layer on a Na grain is darker compared to surrounding materials, since the SEI consists of inorganic compounds (such as  $\text{Na}_2\text{CO}_3$ , NaF, NaOH,  $\text{Na}_2\text{O}$ ) [6, 32] with density higher than Na metal (more information on SEI and Na metal is shown later). We trace the growth rate of a Na grain along different directions where the SEI thickness varies (Fig. 3, also see Movie S2). When the SEI layer is thin, fast growth is observed. As the SEI thickness increases, Na deposition slows down. When the SEI thickness reaches about 130 nm, the Na grain almost stops growing. These observations suggest that  $\text{Na}^+$  ions can penetrate through a thin SEI layer up to a certain thickness. Eventually, the Na grain develops asymmetrically when the SEI layer thickness on the Na grain is not uniform. Although the plots of “growth rate vs SEI thickness” vary for different Na grains, they show a similar trend (Fig. S1 and S2, also see Movie S2, S3). Therefore, SEI has significant impact on the behavior of Na deposition.

### *3.2. Na electrodeposition on an electrode with sharp curvature*

Nucleation and growth of Na grains on the Ti electrode with sharp surface curvature are demonstrated in Fig. 4 (also see Movie S4 and Fig. S3). The electrode regions of high curvature produce an enhanced electric field [33], which can affect the local ion distribution. Thus, characteristics of Na deposition on the electrode with sharp surface curvatures are more dramatic. As shown in Fig. 4A, the surface of the nodule is smooth at the beginning. As the voltage reaches



-2.17 V (43.5 s), a Na grain emerges on the nodule and subsequently grows into an agglomeration of several grains. Individual Na grains are much smaller than the grains grown on the flat electrode. Dendrites (branches) on top of the grains are also observed. The Na deposition proceeds rapidly and the newly deposited Na accumulates mostly at the base of existing grains close to the electrode (“base growth”) leading to an explosive growth behavior (Movie S4). Na deposits not only grow in the vertical direction but also expand in the lateral direction which is accompanied by grains merging together (81.5 s). The growth on the side of electrode is slower due to a weaker local electric field.

At 89.5 s, simultaneous with Na deposition, the outer layer of the Na deposits starts to dissolve (marked with yellow dashed circles). It is interesting that dissolution of Na may occur under a negative potential (-3.54 V) while Na deposition maintains. We consider that since each Na grain is covered with an SEI layer, the electron conductivity of the agglomerated Na grains is poor. Thus, the electric potential at the top of agglomerated Na grains may decrease significantly. Additionally, the base growth of Na grains constantly pushes the existing Na grains up, which may induce mechanical stress and breakdown of the SEI [34-36] thus exposing fresh Na directly to the electrolyte. The high reactivity of Na metal may also lead to Na reacting with electrolyte [14, 34]. The concurrence of dissolution (reaction) and deposition may result in a battery with lower capacity than the theoretical value. As the voltage reaches close to 0 V, no further deposition can be observed and the Na grains start to collapse (marked with yellow arrows indicating the collapsing direction at 119.50 s). Fig. 4B shows more details of the early stage deposition of Na grains on another nodule, which also shows “base growth” behavior. The corresponding applied electrical potential and the measured electrical current over time are shown in Fig. 4C. And, the

trajectories of growth and dissolution of the electrodeposited Na aggregates are plotted as a function of time on both nodules in Fig. 4D.

### *3.3. Evaluation of electron beam effects*

To confirm that Na deposition is not caused by e-beam irradiation, we have conducted control experiments with the same low electron beam dose ( $< 1 \text{ e}\text{\AA}^{-2}\text{s}^{-1}$ ) without applying a cyclic voltammetry. No reaction occurs under such a low beam intensity even for an extended period of time. Furthermore, we did experiments by periodically blocking the beam and no obvious difference in the Na deposition behavior was observed. For more quantitative understanding of the electron beam interaction with the electrolyte and its impacts on the electrodeposition, systematic study of the Na growth under various high electron dose is needed. However, based on our controlled experiments, we can conclude that the electron beam effect under such low dose conditions is insignificant.

### *3.4. Chemical analysis of Na deposits and SEI*

We examine the Na deposits by high angle annular dark field (HAADF) scanning TEM (STEM) imaging and EDS elemental mapping. For these measurements, we stop the reaction before the Na grains are completely dissolved and dry the electrochemical cell without exposing the Na deposits to air. As shown in Fig. 4E, a strong Na signal is observed and other species, such as C, F and P, are also seen. The EDS line scan spectra (Fig. S4) indicate the distribution of F is similar to that of Na, while there are more C and P in the outer layer of the deposits (probably induced by the process of electrolyte drying). Such elemental analysis results are consistent with the granular structure of Na deposits. It is noted that the resolution of EDS maps does not allow

us to distinguish the details of SEI in an individual Na grain. However, the distributions of Na, C and F within the deposits are consistent with the fact that the deposits contain both Na metal and the SEI consists of organic/inorganic compounds, such as organic species of  $\text{ROCO}_2\text{Na}$ ,  $\text{CH}_3\text{ONa}$ ,  $(\text{CH}_2\text{OCO}_2\text{Na})_2$  and inorganic species of  $\text{Na}_2\text{CO}_3$ ,  $\text{NaF}$ ,  $\text{NaOH}$ ,  $\text{Na}_2\text{O}$  [6, 32, 37]. This is further confirmed by *in-situ* x-ray absorption spectroscopy (XAS). By monitoring the chemical state changes of Na during electrochemical deposition of Na, characteristic features of both Na metal and Na complex in Na K-edge XAS are observed (Fig. S5).

### 3.5. Effects of electrode surface roughness and SEI

The above experiments demonstrate that both electrode surface roughness and SEI strongly influence the Na electrodeposition. Fig. 5A-C highlights the base growth behavior of Na grain growth on the sharp curved electrode. Nano-sized Na grains are explosively grown at the tip of the sharp electrode. Once a Na grain is deposited, it reacts with the electrolyte [38] and an SEI layer is formed on the surface. As the SEI layer thickens, the Na grain growth slows down. Further deposition of Na proceeds through Na ion diffusion from the electrolyte solution to the electrode, resulting in the growth of new Na grains. The emerging Na grains push the existing Na grains up to form base growth, especially when the electric field is localized. We consider the growth behavior of Na on the electrode with sharp curvature is directed by the local accumulated current density. The high current density introduces more nucleation of Na. However, the underlying mechanisms of SEI impacts on the observed based growth behavior is not obvious. In the following, we evaluate the transport limitations observed in the SEI associated with Na metal deposition using a continuum-based computational model.

We develop a continuum-based computational model by considering the conduction of metal ions and diffusion of electrolyte salt [39, 40]. This model captures the movement of metal ions in both the electrolyte and SEI layers. The equations used for modeling the migration of metal ions and diffusion of electrolyte salt is derived based on the Concentrated Solution Theory (CST), pioneered by John Newman and coworkers [39, 41]. The oxidation/reduction reaction is assumed to occur at the electrode/electrolyte or electrode/SEI interface. The reaction current is estimated based on the highly nonlinear Butler-Volmer equation [39]. The developed model (see details in Supplementary Materials) is used to understand the current density at the tip ( $i_{tip}$ ) and base ( $i_{base}$ ) of metal deposits. If the magnitude of reaction current at the tip is larger than that at the base ( $i_{tip} > i_{base}$ ), tip growth of metallic deposits is expected to occur. Whereas, if the reaction current at the base is larger in magnitude than the tip region ( $i_{base} > i_{tip}$ ), base growth is favorable.

A schematic diagram of a metal deposit, and the corresponding SEI layer is demonstrated in Fig. 6A. The two electrodes are located at the bottom and top of the computational domain with a fixed distance apart from each other. Metal deposition occurs at the top electrode while dissolution happens at the bottom electrode. Based on the experimental observations, we assume the average SEI thickness of 80 nm in the schematic diagram shown in Fig. 6A. And, a layered SEI structure [31, 39, 42] with a dense inorganic layer (15%) adjacent to the electrode and a porous organic layer (85%) residing close to the electrolyte is proposed for the calculation (see more details in Supplementary Materials). Additionally, a current density of 100 A/m<sup>2</sup> is applied at the bottom electrode (Supplementary Materials). The current density at the top electrode is smaller than that applied at the bottom and it varies when different diffusion coefficient is incorporated (Fig. 6B and 6C). For example, if the metal ion diffusivity within the SEI layer is one order of magnitude

smaller than that in the liquid electrolyte, the SEI layer does not impart a large resistance to the transport of metal cations, and enhanced deposition at the tip of the protrusion is still possible, as demonstrated in Fig. 6B. However, if metal ion diffusivity within the SEI layer is six orders of magnitude smaller than the liquid electrolyte, it is evident from Fig. 6C that due to enhanced transport limitations, deposition at the base is preferred. Thus, a transition of metal deposition from tip to base can be observed by increasing the transport limitations of metal ions through the SEI layer.

To elucidate the combined effects of thickness and transport properties of the SEI layer on the Na metal deposition process, a phase map is developed (Fig. 6D), where the ratio of the reaction current between the tip and base ( $i_{tip}/i_{base}$ ) is plotted as a function of “SEI thickness” and “SEI diffusivity”. The metal ion diffusion coefficient through the SEI layer is normalized by dividing the metal ion diffusivity in the SEI layer by that in the liquid electrolyte ( $D_{SEI}/D_{Elec}$ ). As SEI consists of a dense inorganic layer and a porous organic layer [31, 39], and the diffusion coefficient through SEI is modified for preparing the phase map (see Supplementary Materials). As shown in Fig. 6D, the yellow region under high SEI diffusivities and thin SEI thickness indicates the combination of parameters where tip deposition is favorable. The green/blue region observed under low diffusion coefficients and thick SEI layers indicates conditions where base deposition is favorable. Diffusion coefficient of lithium through the SEI layer can be assumed to be around five to six orders of magnitude smaller than that within liquid electrolytes [43] ( $(D_{SEI}/D_{Elec}) \sim 10^{-5} - 10^{-6}$ ). The diffusion coefficient of Na through the SEI layer is an unknown quantity, which can be higher [44] (due to smaller solvation shell) or lower (due to larger atomic radius) than that observed for Li. If we assume the similar diffusivity of Na through the SEI layer as that of Li, the thick SEI layer on Na deposits may lead to difficulties of Na ions

transport within the Na-SEI layer and thus the base growth behavior. In addition, the variation on electrode's radius of curvature can also affect the Na deposition behavior, as compared with Fig.4A and Fig.2A, which is closely related with the current density (Fig. S6). Another interesting phenomenon is the asymmetric deposition and nonuniform growth of the deposit (Fig. 3), the simulation indicates it is attributed to the local SEI thickness variation (Fig. S7).

The transition from tip growth to base deposition can be characterized by “stability limit”, as shown in Fig. S8. In the phase map (Fig. 6D), layered SEI with 15% the dense inorganic layer and 85% porous organic layer is used [42]. Changing the relative amount of dense inorganic layer can significantly alter the stability limit. This aspect has been clearly demonstrated in Fig. S8 by comparing the stability limits for 15-85 and 40-60 divisions of the inorganic-organic layers [42]. The 15% inorganic and 85% organic components that are adopted in Fig. 6D provides the best correlation with experimental observations of base deposition within thick Na-SEI layers. Future high-resolution structural characterization of the Na SEI layers on individual Na grains will be valuable.

#### 4. Conclusions

In conclusion, we have investigated the effects of electrode surface roughness on the Na electrodeposition. Our study using *in-situ* liquid phase TEM in combination with other complementary methods and continuum-based computational modelling reveals the contribution of the electrode surface roughness to the different dynamic growth behavior of Na and grain morphology, where SEI on each individual grain plays an important role. The non-uniform thickness of SEI on a single Na grain leads to different local growth rates and uneven surface morphology. The drastic “base growth” of Na with smaller grains is distinct on the sharp curved

electrode, where the concurrence of Na dissolution with the Na deposition has also been observed. Given the explosive Na deposition on the rough electrode surface compared to that on the flat electrode, microscopic smooth electrode surface is preferred to limit the inhomogeneous Na growth or dendrite formation. Unveiling the electrochemical deposition behaviors of Na on the different electrode roughness and SEI effects opens the opportunity for future electrode engineering with improved device performance.

### **Acknowledgments:**

This work was supported by the U.S. Department of Energy (DOE), Office of Science, Office of Basic Energy Sciences (BES), Materials Sciences and Engineering Division under Contract No. DE-AC02-05-CH11231 within the *in-situ* TEM program (KC22ZH). The work at the Molecular Foundry and the XAS experiments at the Advanced Light Source in Lawrence Berkeley National Laboratory (LBNL) were supported by DOE BES under Contract # DE-AC02-05CH11231. X. W. Zhang acknowledges the support of National Basic Research Program of China (2013CB632101) and China Scholarship Council under No.201406190080. S.-Y.L. was supported by an LDRD project at LBNL.

### **Conflicts of Interest**

The authors declare that they have no competing financial interests.

### **References**

- [1] J.B. Goodenough, Y. Kim, Challenges for Rechargeable Li Batteries, *Chemistry of Materials*, 22 (2010) 587-603.
- [2] M. Armand, J.M. Tarascon, Building better batteries, *Nature*, 451 (2008) 652-657.

- [3] S.W. Kim, D.H. Seo, X.H. Ma, G. Ceder, K. Kang, Electrode Materials for Rechargeable Sodium-Ion Batteries: Potential Alternatives to Current Lithium-Ion Batteries, *Advanced Energy Materials*, 2 (2012) 710-721.
- [4] X.B. Cheng, R. Zhang, C.Z. Zhao, Q. Zhang, Toward Safe Lithium Metal Anode in Rechargeable Batteries: A Review, *Chemical Reviews*, 117 (2017) 10403-10473.
- [5] H.D. Abruna, Editorial: Advances in Functional Electrodes, *Electrochemistry*, 87 (2019) 107-107.
- [6] A. Ponrouch, E. Marchante, M. Courty, J.-M. Tarascon, M.R. Palacin, In search of an optimized electrolyte for Na-ion batteries, *Energy & Environmental Science*, 5 (2012) 8572-8583.
- [7] A. Ponrouch, R. Dedryvere, D. Monti, A.E. Demet, J.M. Ateba Mba, L. Croguennec, C. Masquelier, P. Johansson, M.R. Palacin, Towards high energy density sodium ion batteries through electrolyte optimization, *Energy & Environmental Science*, 6 (2013) 2361-2369.
- [8] M.D. Slater, D. Kim, E. Lee, C.S. Johnson, Sodium-Ion Batteries, *Advanced Functional Materials*, 23 (2013) 947-958.
- [9] H.L. Pan, Y.S. Hu, L.Q. Chen, Room-temperature stationary sodium-ion batteries for large-scale electric energy storage, *Energy & Environmental Science*, 6 (2013) 2338-2360.
- [10] Y.U. Park, D.H. Seo, H.S. Kwon, B. Kim, J. Kim, H. Kim, I. Kim, H.I. Yoo, K. Kang, A New High-Energy Cathode for a Na-Ion Battery with Ultrahigh Stability, *Journal of the American Chemical Society*, 135 (2013) 13870-13878.
- [11] B. Sun, P. Xiong, U. Maitra, D. Langsdorf, K. Yan, C.Y. Wang, J. Janek, D. Schroder, G.X. Wang, Design Strategies to Enable the Efficient Use of Sodium Metal Anodes in High-Energy Batteries, *Adv Mater*, (2019).
- [12] B. Lee, E. Paek, D. Mitlin, S.W. Lee, Sodium Metal Anodes: Emerging Solutions to Dendrite Growth, *Chem Rev*, 119 (2019) 5416-5460.
- [13] K. Xu, Electrolytes and Interphases in Li-Ion Batteries and Beyond, *Chemical Reviews*, 114 (2014) 11503-11618.
- [14] Y.S. Hong, N. Li, H.S. Chen, P. Wang, W.L. Song, D.N. Fang, In operando observation of chemical and mechanical stability of Li and Na dendrites under quasi-zero electrochemical field, *Energy Storage Materials*, 11 (2018) 118-126.
- [15] R. Dugas, A. Ponrouch, G. Gachot, R. David, M.R. Palacin, J.M. Tarascon, Na Reactivity toward Carbonate-Based Electrolytes: The Effect of FEC as Additive, *J Electrochem Soc*, 163 (2016) A2333-A2339.
- [16] Y. Zhao, K.R. Adair, X.L. Sun, Recent developments and insights into the understanding of Na metal anodes for Na-metal batteries, *Energ Environ Sci*, 11 (2018) 2673-2695.
- [17] Y.L. Xu, A.S. Menon, P.P.R.M.L. Harks, D.C. Hermes, L.A. Haverkate, S. Unnikrishnan, F.M. Mulder, Honeycomb-like porous 3D nickel electrodeposition for stable Li and Na metal anodes, *Energy Storage Materials*, 12 (2018) 69-78.
- [18] W. Luo, Y. Zhang, S.M. Xu, J.Q. Dai, E. Hitz, Y.J. Li, C.P. Yang, C.J. Chen, B.Y. Liu, L.B. Hu, Encapsulation of Metallic Na in an Electrically Conductive Host with Porous Channels as a Highly Stable Na Metal Anode, *Nano Lett*, 17 (2017) 3792-3797.
- [19] S. Liu, S. Tang, X.Y. Zhang, A.X. Wang, Q.H. Yang, J.Y. Luo, Porous Al Current Collector for Dendrite-Free Na Metal Anodes, *Nano Lett*, 17 (2017) 5862-5868.
- [20] Y.Y. Lu, Q. Zhang, M. Han, J. Chen, Stable Na plating/stripping electrochemistry realized by a 3D Cu current collector with thin nanowires, *Chem Commun*, 53 (2017) 12910-12913.
- [21] S.Y. Wei, S. Choudhury, J. Xu, P. Nath, Z.Y. Tu, L.A. Archer, Highly Stable Sodium Batteries Enabled by Functional Ionic Polymer Membranes, *Adv Mater*, 29 (2017).



- [22] S.Q. Shi, P. Lu, Z.Y. Liu, Y. Qi, L.G. Hector, H. Li, S.J. Harris, Direct Calculation of Li-Ion Transport in the Solid Electrolyte Interphase, *J Am Chem Soc*, 134 (2012) 15476-15487.
- [23] Q. Li, S.P. Zhu, Y.Y. Lu, 3D Porous Cu Current Collector/Li-Metal Composite Anode for Stable Lithium-Metal Batteries, *Adv Funct Mater*, 27 (2017).
- [24] A.X. Wang, Q.B. Deng, L.J. Deng, X.Z. Guan, J.Y. Luo, Eliminating Tip Dendrite Growth by Lorentz Force for Stable Lithium Metal Anodes, *Adv Funct Mater*, 29 (2019).
- [25] F.M. Ross, Opportunities and challenges in liquid cell electron microscopy, *Science*, 350 (2015) 10.
- [26] M.E. Holtz, Y.C. Yu, D. Gunceler, J. Gao, R. Sundararaman, K.A. Schwarz, T.A. Arias, H.D. Abruna, D.A. Muller, Nanoscale Imaging of Lithium Ion Distribution During In Situ Operation of Battery Electrode and Electrolyte, *Nano Lett*, 14 (2014) 1453-1459.
- [27] Z.Y. Zeng, W.I. Liang, H.G. Liao, H.L.L. Xin, Y.H. Chu, H.M. Zheng, Visualization of Electrode-Electrolyte Interfaces in LiPF<sub>6</sub>/EC/DEC Electrolyte for Lithium Ion Batteries via in Situ TEM, *Nano Letters*, 14 (2014) 1745-1750.
- [28] Z. Zeng, W.-I. Liang, Y.H. Chu, H. Zheng, FD 176: In Situ TEM Study of Li-Au Reaction in an Electrochemical Liquid Cell, *Faraday Discussions*, 176 (2014) 95-107.
- [29] A. Kushima, K.P. So, C. Su, P. Bai, N. Kuriyama, T. Maebashi, Y. Fujiwara, M.Z. Bazant, J. Li, Liquid cell transmission electron microscopy observation of lithium metal growth and dissolution: Root growth, dead lithium and lithium flotsams, *Nano Energy*, 32 (2017) 271-279.
- [30] B.S. Parimalam, A.D. MacIntosh, R. Kadam, B.L. Lucht, Decomposition Reactions of Anode Solid Electrolyte Interphase (SEI) Components with LiPF<sub>6</sub>, *Journal of Physical Chemistry C*, 121 (2017) 22733-22738.
- [31] D. Aurbach, Review of selected electrode–solution interactions which determine the performance of Li and Li ion batteries, *Journal of Power Sources*, 89 (2000) 206-218.
- [32] M. Moshkovich, Y. Gofer, D. Aurbach, Investigation of the electrochemical windows of aprotic alkali metal (Li,Na,K) salt solutions, *Journal of the Electrochemical Society*, 148 (2001) E155-E167.
- [33] M. Liu, Y. Pang, B. Zhang, P. De Luna, O. Voznyy, J. Xu, X. Zheng, C.T. Dinh, F. Fan, C. Cao, F.P.G. de Arquer, T.S. Safaei, A. Mepham, A. Klinkova, E. Kumacheva, T. Filleter, D. Sinton, S.O. Kelley, E.H. Sargent, Enhanced electrocatalytic CO<sub>2</sub> reduction via field-induced reagent concentration, *Nature*, 537 (2016) 5.
- [34] Z.W. Seh, J. Sun, Y. Sun, Y. Cui, A Highly Reversible Room-Temperature Sodium Metal Anode, *ACS Central Science*, 1 (2015) 449-455.
- [35] D. Aurbach, E. Zinigrad, Y. Cohen, H. Teller, A short review of failure mechanisms of lithium metal and lithiated graphite anodes in liquid electrolyte solutions, *Solid State Ionics*, 148 (2002) 405-416.
- [36] S. Komaba, W. Murata, T. Ishikawa, N. Yabuuchi, T. Ozeki, T. Nakayama, A. Ogata, K. Gotoh, K. Fujiwara, Electrochemical Na Insertion and Solid Electrolyte Interphase for Hard-Carbon Electrodes and Application to Na-Ion Batteries, *Advanced Functional Materials*, 21 (2011) 3859-3867.
- [37] M. Dahbi, N. Yabuuchi, M. Fukunishi, K. Kubota, K. Chihara, K. Tokiwa, X.-f. Yu, H. Ushiyama, K. Yamashita, J.-Y. Son, Y.-T. Cui, H. Oji, S. Komaba, Black Phosphorus as a High-Capacity, High-Capability Negative Electrode for Sodium-Ion Batteries: Investigation of the Electrode/Electrolyte Interface, *Chemistry of Materials*, 28 (2016) 1625-1635.

- [38] B. Philippe, M. Valvo, F. Lindgren, H. Rensmo, K. Edstrom, Investigation of the Electrode/Electrolyte Interface of Fe<sub>2</sub>O<sub>3</sub> Composite Electrodes: Li vs Na Batteries, *Chemistry of Materials*, 26 (2014) 5028-5041.
- [39] J. Christensen, J. Newman, A mathematical model for the lithium-ion negative electrode solid electrolyte interphase, *Journal of the Electrochemical Society*, 151 (2004) A1977-A1988.
- [40] C. Monroe, J. Newman, Dendrite growth in lithium/polymer systems - A propagation model for liquid electrolytes under galvanostatic conditions, *Journal of the Electrochemical Society*, 150 (2003) A1377-A1384.
- [41] J.S. Newman, K.E. Thomas-Alyea, *Electrochemical systems*, 3rd ed., J. Wiley, Hoboken, N.J., 2004.
- [42] P.J. Guan, L. Liu, X.K. Lin, Simulation and experiment on solid electrolyte interphase (SEI) morphology evolution and lithium-ion diffusion, *Journal of the Electrochemical Society*, 162 (2015) A1798-A1808.
- [43] L. Benitez, J.M. Seminario, Ion diffusivity through the solid electrolyte interphase in lithium-ion batteries, *Journal of the Electrochemical Society*, 164 (2017) E3159-E3170.
- [44] T.A. Pham, K.E. Kweon, A. Samanta, V. Lordi, J.E. Pask, Solvation and dynamics of sodium and potassium in ethylene carbonate from ab initio molecular dynamics simulations, *Journal of Physical Chemistry C*, 121 (2017) 21913-21920.

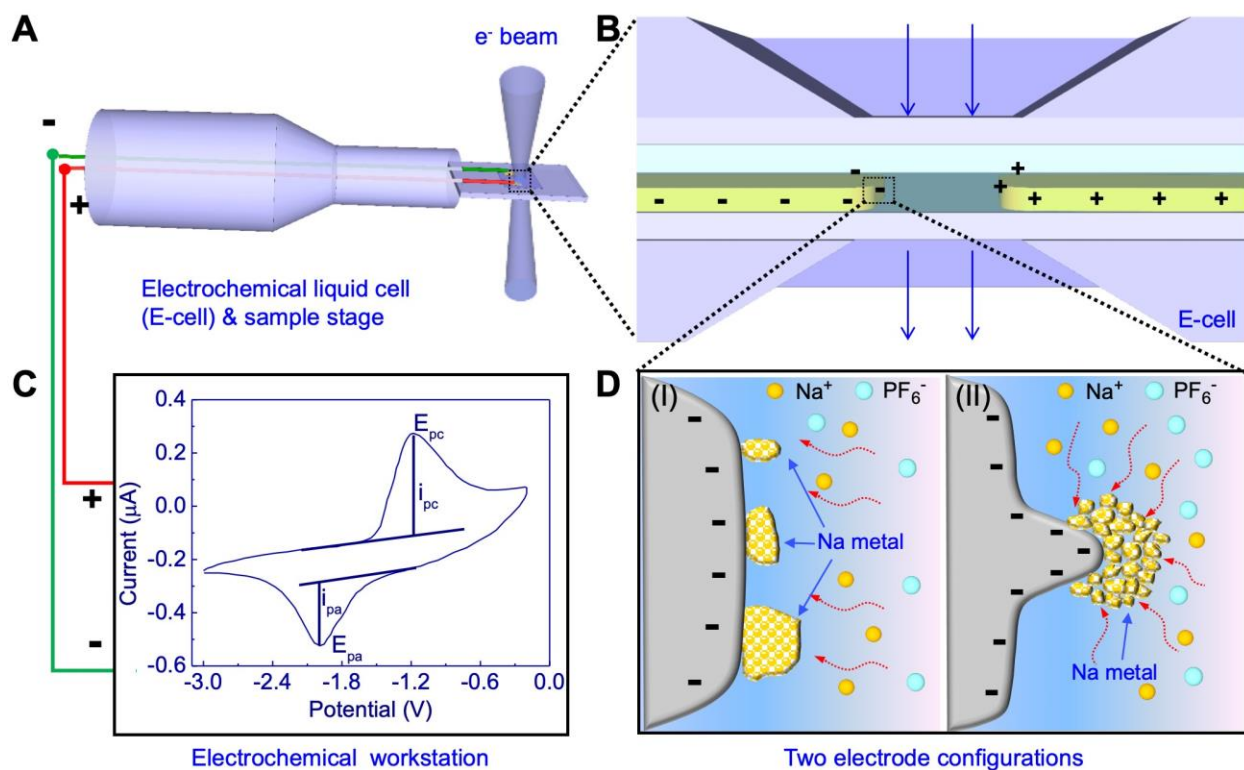


**Fig. 1. A schematic of the experimental setup for *in-situ* TEM study of Na electrochemical deposition.** (A) A custom-made electrochemical TEM sample stage. (B) An electrochemical liquid cell that fits the sample stage in (A). (C) An electrochemical program is applied to the electrochemical cell using an electrochemical workstation. (D) *In-situ* imaging of the electrochemical deposition of Na on the Ti electrode with different configurations composing of flat (I) or sharp (II) curvature.

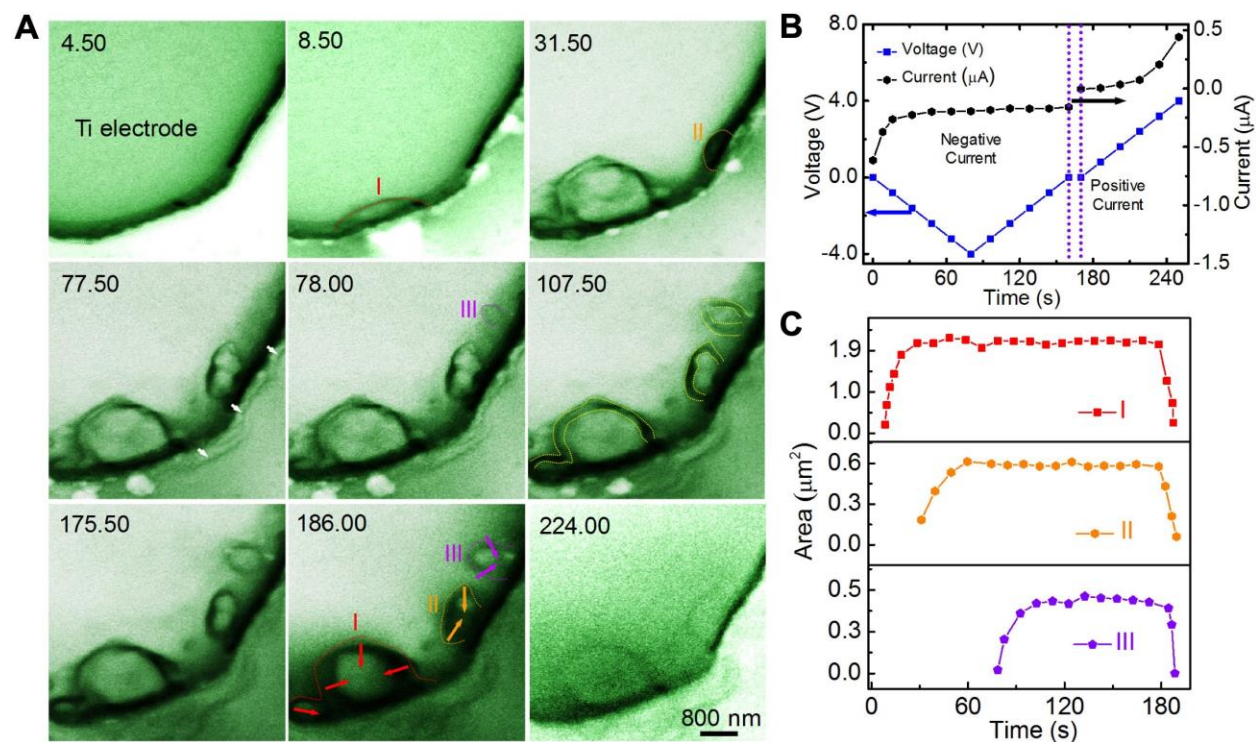


**Fig. 2. Nucleation and growth of Na on a flat Ti electrode, where size and shape evolution of three Na grains during a charge cycle is highlighted.** (A) Sequential TEM images show the nucleation and growth of Na grains under a negative potential (from the initial frame to the frame marked with 175.50 s) and the dissolution of Na grains (frame 186.00 s and after). (B) The applied electric potential and measured electric current corresponding to (A). (C) The projected area of individual Na metal grains (as labeled in (A)) as a function of time during cyclic voltammetry in the voltage range of 0 to -4 V at scan rate of 0.05 V/s.

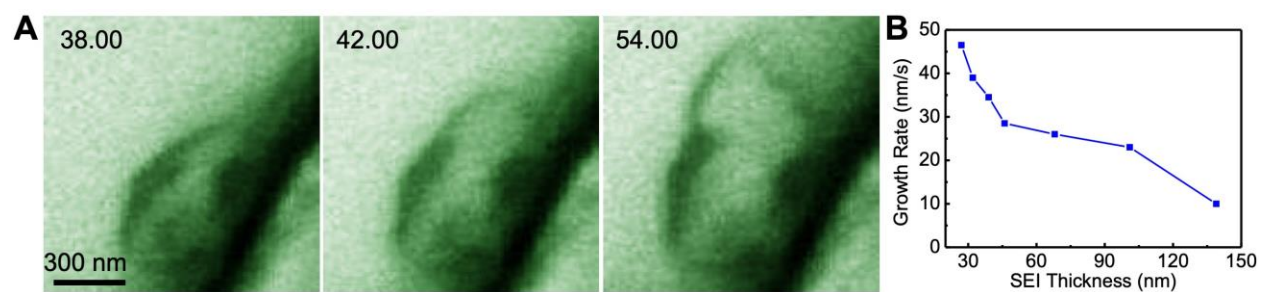


**Fig. 3. Na grain growth rate versus SEI thickness.** (A) Sequential images show the growth of a Na grain. (B) Growth rate of the Na grain as a function of SEI layer thickness. The growth rate and SEI thickness were estimated at different locations of the Na grain (see more details of the measurements in Fig. S1 and S2).

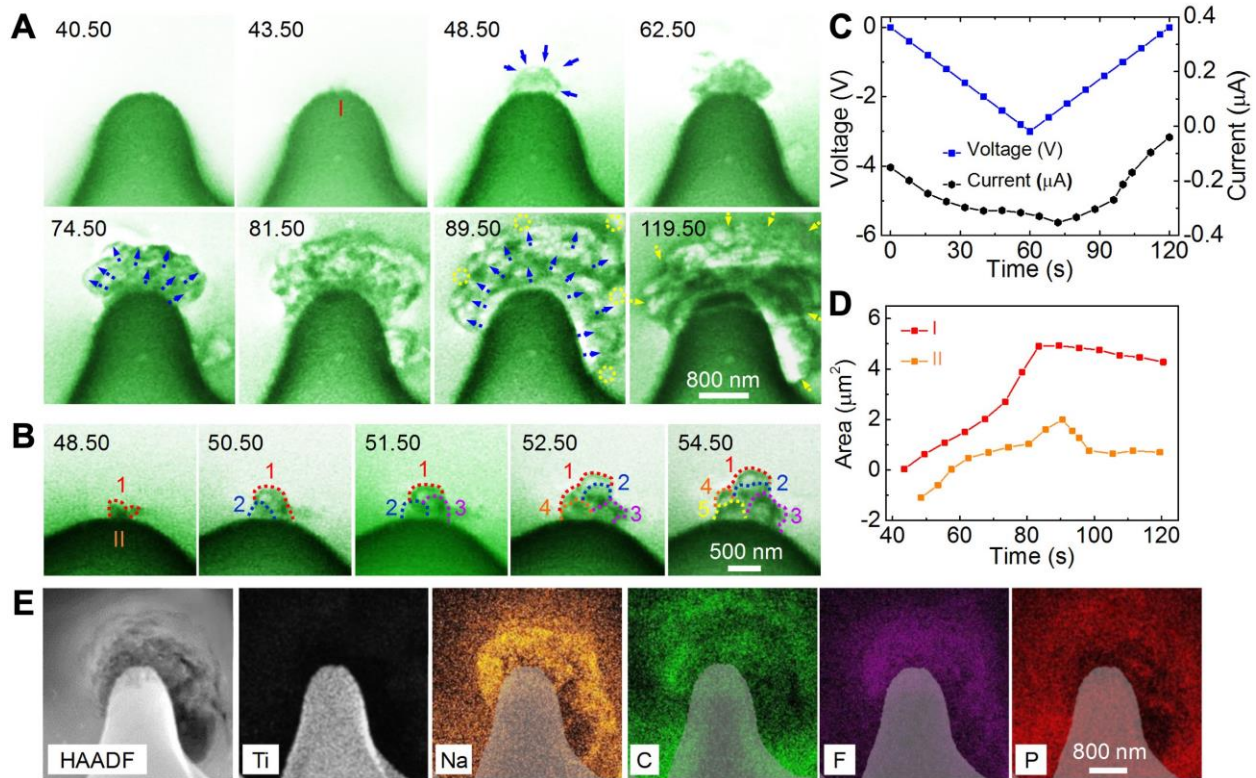


**Fig. 4. Nucleation and growth of Na on Ti electrode with sharp curvature.** (A) Sequential TEM images show the base-growth of Na on a nodule of Ti electrode, where the growth is focused at the point with highest curvature. The blue arrows correspond to the moving direction of Na grains during deposition, the yellow circles correspond to the dissolution of Na, and the yellow arrows correspond to the direction of collapsing Na grains. (B) The initial deposition of Na grains on another nodule on Ti electrode with high curvature indicating the base growth behavior. (C) The applied electric potential and measured electric current. (D) Whole area evolution of Na grain aggregates labeled in (A) and (B) as a function of time during cyclic voltammetry in the voltage range of 0 to -3 V with a scan rate of 0.05 V/s. (E) HAADF image and EDS elemental maps showing Ti, Na, C, F and P distribution, which were obtained from the same electrochemical cell after drying under inert conditions.



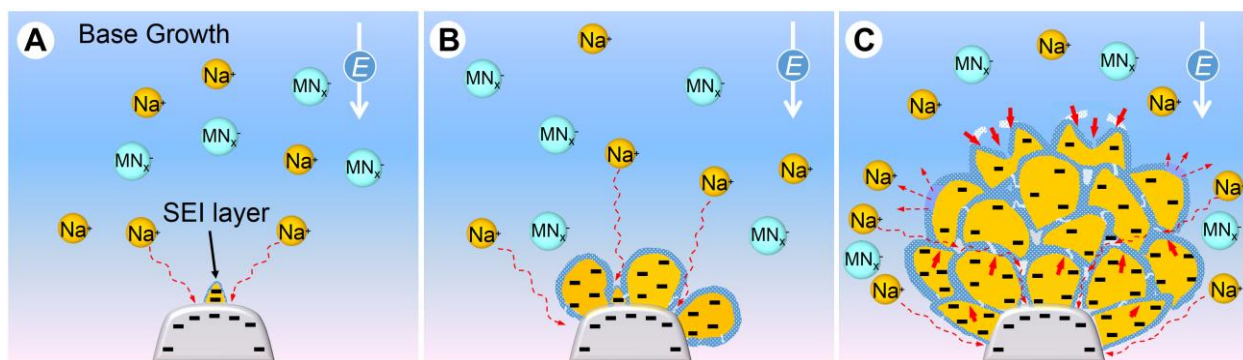


**Fig. 5. Schematic illustrations of Na growth behaviors on the sharp curved electrode. (A-C)**

The newly formed Na grains prefer to nucleate at the base close to the electrode. The sequential deposition of Na grains and the later stage dissolution at the top of deposit are demonstrated. The SEI layer on each individual Na grain (yellow) is highlighted in blue.

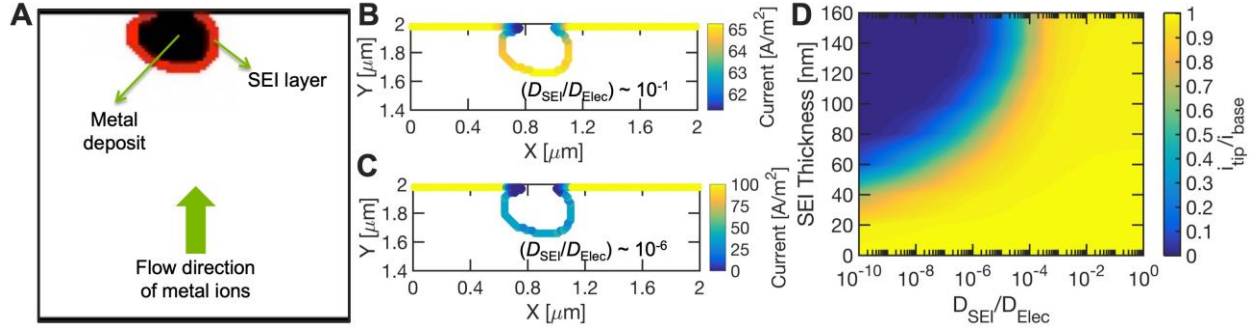


**Fig. 6. Computational analysis demonstrating the SEI effects on the electrodeposition of alkali metal.** (A) A schematic diagram of the computational domain adopted for the analysis. The metal deposit is denoted by the black color, and the SEI layer is depicted by red. The bottom and top electrodes (thick black lines) are  $2.0 \mu\text{m}$  from each other. (B) Metal deposition occurs at the tip of protrusion when metal ion transport through the SEI layer is fast. SEI diffusivity is one order of magnitude smaller than that observed in electrolyte ( $D_{SEI}/D_{Elec} \sim 10^{-1}$ ). (C) Metal deposition is preferred at the base when ion transport through the SEI layer is slow. SEI diffusivity is six orders of magnitude smaller than that observed in liquid electrolyte ( $D_{SEI}/D_{Elec} \sim 10^{-6}$ ). (D) A phase map between “SEI thickness” and “SEI diffusivity” (normalized as the ratio of diffusivity between SEI and electrolyte ( $D_{SEI}/D_{Elec}$ )) demonstrates the regions where enhanced deposition should occur at the tip (yellow region), and where metal should be plated at the base (green/blue portion). For Na deposition, thickness of the SEI layer range between 100-140 nm, but diffusivity of Na through the SEI layer is unknown. Under the assumption of similar Na diffusivities through the SEI layer with Li ( $(D_{SEI}/D_{Elec}) \sim 10^{-5} - 10^{-6}$ ), base growth for Na deposition is favorable.